REVISED VERSION ae-2020-00069y

OER Performances of Cationic Substituted (100)-Oriented IrO_2 Thin Films: A Joint Experimental and Theoretical Study

Gaëtan Buvat [1,5] ¶, Mohammad J. Eslamibidgoli [1,2] ¶, Sébastien Garbarino [3],
Michael Eikerling [4], Daniel Guay [1] *

[1] INRS-Énergie, Matériaux Télécommunications
1650 Lionel-Boulet Boulevard, P.O. 1020,
Varennes, QC, Canada J3X 1S2

[2] Department of Chemistry, Simon Fraser University,
8888 University Drive, Burnaby, BC, Canada V5A 1S6

[3] PRIMA Québec, 505 Boulevard Maisonneuve Ouest,
Montréal, QC H3A 3C2, Canada

[4] IEK-13, Institute of Energy and Climate Research,
Forschungszentrum Jülich GmbH, 52425 Jülich, Germany

[5] Current address: Institut d'Electronique, de Microélectronique et de Nanotechnologie
(IEMN), CNRS UMR 8520 – Université de Lille Sciences et Technologies, BP60069,
Villeneuve d'Ascq cedex, France

¶ These authors contribute equally to the work
* To whom correspondence should be sent: guay@emt.inrs.ca

Abstract

Cationic substitution was investigated as a strategy to increase the electrocatalytic activity of IrO_2-based films for the oxygen evolution reaction. For this purpose, an approach that combines detailed experimental characterization with quantum mechanical calculation based on density functional theory was employed. A series of (100)-oriented $Ir_{1-x}M_xO_2$ thin films, with M = Ni, Cr, Mo, W, Sn, Pt, Rh, Ru, V and Mn, was prepared with a one-step synthesis approach based on pulsed laser deposition and the electrocatalytic activity of these films for the OER was measured. Matching materials compositions and structures were generated *in silico* for DFT-based calculations of their electronic structure and OER pathway. Comparison of experimental and theoretical results reveals the viable activity descriptor, paving the way for a systematic search to find the most active Ir-based OER catalyst.

Keywords

Oxygen Evolution Reaction, IrO_2, Pulsed Laser Deposition, DFT calculation, epitaxy, doping.

1. Introduction

Over more than a century, carbon-based fossil fuels have been the feedstock of the fast-paced techno-economic development in industrialized countries. However, the depletion of fossil fuel resources as well as the environmental pollution and fatal accumulation of CO_2 associated with their excessive exploitation drive efforts to develop more sustainable and green energy sources [1-3]. Wind energy, solar energy, tidal energy, and hydroelectricity are sustainable and renewable energy sources, but the intermittency of electricity generation and the partial incompatibility with typical energy demand patterns constitute a formidable demand-supply challenge. In order to convert renewably generated electricity and afford large-scale and long-term energy storage, electrolysis of water to produce hydrogen (and oxygen) is becoming a promising if not compulsory element of the renewable energy cycle.

The electrolytic generation of hydrogen is limited by the anode reaction, where the Oxygen Evolution Reaction (OER) occurs. Four electrons and protons are transferred during the OER, and the reaction is sluggish and requires efficient electrocatalytic materials to proceed at sufficient rates [4, 5]. Iridium oxide is one of the best materials for the OER [6-8]. However, Ir is an expensive noble metal and it ranges among the least-abundant elemental materials in the upper crust of the Earth [9]. Accordingly, considerable research efforts have been devoted to reduce its use via identifying suitable replacement materials or boosting the intrinsic electrocatalytic OER activity of Ir-based materials with the help of suitable strategies in materials design and fabrication.

The (110) facet of IrO_2 exhibits the highest thermodynamic stability, but the (100) facet displays the highest activity for the OER in alkaline electrolyte [10]. Nevertheless, it is known from modelling that the binding energies of the oxygen intermediates (*O, *OH and *OOH) involved in the OER on IrO_2 are not optimal [11]. It is known that a surface with weaker binding of the *OH reaction intermediate would lower the onset potential and thus enhance the activity of the OER. Alloying provides a primary avenue to tune the binding energy of reaction intermediates and increase the intrinsic activity of materials [12-14]. This approach was followed in the development of improved electrocatalysts for the oxygen reduction reaction in fuel cells [15-17]. In that case, the strategy pursued involved a combination of modeling and experimental studies of well-defined systems with specific surface orientations; it has furthered the understanding of the relation between alloying and intrinsic activity [18].

For the OER, only few experimental studies have been undertaken to determine the effect of alloying on the intrinsic OER activity of the most active (100)-oriented facet of IrO_2, and many studies have dealt with less well defined systems. In the literature, several IrO_2-MO_x composite and/or mixed systems have been investigated, including NiO_x [19], MnO_x [20, 21], MoO_3 [22], SnO_2 [23-25] and WO_3 [26, 27]. Hybrid IrO_x/RuO_x thin films were investigated, with submonolayer amounts of IrO_x deposited on top of a RuO_x thin film [28]. Studies of $Ir_{1-x}M_xO_2$ solid solutions were reported as well, with M = Cr [29], Pt [30], Ru [31, 32], and Sn [33, 34]; yet, conclusive evidence of alloy formation through detailed XRD analysis was not always presented. Co-doping of IrO_2 with Co and Ni has recently been investigated [35].

Another avenue followed was to start with materials made of Ir and M in their metallic states, proceeding from there to investigate the electrocatalytic activity of thermally and/or electrochemically oxidized alloys for the OER. The systems that were investigated following this approach were IrCr [36], IrNi [36-42], IrPt [43], IrRh [44, 45], IrSn [36], IrTi [36], and IrW [46, 47]. In some of these studies, OER performances better than IrO_2 were demonstrated, and modelling was used to provide a theoretical basis to this betterment of the OER characteristics. However, DFT modeling of electrocatalytic surfaces was usually performed for slab-like geometries of regularly spaced atoms with specific and well-defined surface terminations. The discrepancies between structures and surface morphologies considered in experiment and DFT-based simulations impair the comparison of results. Extensive characterization of surface compositions and structure of the electrode material under investigation has been used to identify the best slab model to compare with DFT calculations. An interesting alternative would be to synthesize (Ir,M)O_2 oxide alloys with a specific (hkl) surface termination from the start, which can then be reproduced identically with the slab model in DFT calculations. This approach is adopted in this article.

In this study, (100)-oriented epitaxial (Ir,M)O_2 thin films were prepared by the pulsed laser deposition (PLD) technique, with M chosen from early (Cr, Mn and Ni) and late (Ru, Rh and Pt) transition metals, post-transition metal (Sn), and high valence dopant elements (W, Mo, V). The intrinsic OER electrocatalytic activity of these films was experimentally determined and compared to results obtained from DFT calculations. The activity trends seen were scrutinized with the help of DFT results and the best alloying elements were identified. This paper is organized as follows. The first section presents and discusses structural data. Thereafter, trends in OER activity will be discussed. A thorough comparison of modelling and experimental results is provided.

2. Results and Discussion

2.1. Bulk structure of iridium-metal mixed oxides

Bulk structure calculations were performed for oxides with composition $Ir_{1-x}M_xO_2$ (see Figure S1), and x values 1/16, 1/8, 3/16, 1/4. Figure 1 shows the lattice parameters a and c of the tetragonal unit cell as a function of x for each oxide material, with M = Cr, Mn, Mo, Ni, Pt, Rh, Ru, Sn, V and W. It is expected that the lattice parameters shrink or expand with the dopant fraction in the oxide alloy based on the relative ionic radius of M with respect to Ir. Figure 2 displays the unit cell volume for each material with stoichiometry $Ir_{0.75}M_{0.25}O_2$ plotted against the difference of their ionic radii (ionic radius of M – ionic radius of Ir, both in +4 oxidation state in an octahedral environment). The volume of the unit cell increases linearly as the radius of the dopant increases.

The present study strives to directly compare results of DFT computations to experimental data. Accordingly, it was critical to identify a synthesis method that allows preparing (100)-oriented rutile-like $Ir_{1-x}M_xO_2$ thin films with the same surface termination and crystalline structure as the slabs used in computations. This was achieved with pulsed laser deposition (PLD). In the past, it has been demonstrated that this deposition technique allows for the preparation of epitaxial IrO_2 and metallic alloy thin films with different (hkl) orientations [10, 48, 49]. Accordingly, (100)-oriented $Ir_{1-x}M_xO_2$ thin films were prepared on (100) $SrTiO_3$ substrate. The thickness of all films was between 23 to 68 nm, and the M content was between 0 and 46 at.% (see Table 1), as a result of variation between the ablation and deposition rates of different metallic elements [50].

The structure and the orientation of $Ir_{1-x}M_xO_2$ thin films was assessed by θ-2θ X-ray diffraction (XRD) and results are shown in Figure 3. All samples exhibit the same XRD pattern. The main peaks at 23° and 47° are the (100) and (200) diffraction peaks of the (100) $SrTiO_3$ substrate, respectively, and the Kβ and WLα reflection of (200) $SrTiO_3$ are seen at 42° and 44°, respectively. The remaining peak near $2\theta = 40^o$ is the (200) plane of rutile $Ir_{1-x}M_xO_2$. The (110) and (101) XRD peak of $Ir_{1-x}M_xO_2$ would have been expected near $2\theta = 28$ and 35°, respectively. These peaks are not observed in any of the $Ir_{1-x}M_xO_2$ thin films, indicating that all films are growing along the [100] orientation that is oriented perpendicularly to the substrate surface. The epitaxy relationship between the IrO_2 film and the $SrTiO_3$ substrate was previously investigated in details using X-ray phi-scan measurements and X-ray reciprocal space mapping [51]. Close inspection of XRD patterns reveals there are no extraneous peaks that could be associated to MO_x oxide compounds. Depending on M, the position of the (200) XRD peak of $Ir_{1-x}M_xO_2$ is shifted with respect to the IrO_2 bulk value. This indicates that dissolution of M in

IrO_2 occurs. The out-of-plane unit cell parameter a was calculated from the 2θ position of the (200) peak, and the results are given in Table 1.

From DFT calculations, we calculated the lattice parameter, a_{DFT} of rutile $Ir_{1-x}M_xO_2$ thin films using the x values measured experimentally for each element. To achieve this, a linear interpolation was performed for each M using the data of Figure 2. Figure 4 plots a_{DFT} over experimentally measured a values. The diagonal line represents a perfect correlation between DFT calculations and experimental values, and most data points lie very close to this line, with the exception of W, revealing, generally, a good correlation between experimental and *in silico* structures. This is a further evidence that $Ir_{1-x}M_xO_2$ solid solutions are formed instead of $IrO_2{\bullet}MO_x$ mixtures of oxides. We conclude that the PLD technique enables the substitution of Ir by a large array of elements (M) in the rutile structure of IrO_2. This can be accomplished while preserving the (100) film orientation. In the following, we will investigate the electrochemical characteristics of (100)-oriented $Ir_{1-x}M_xO_2$ thin films for the OER.

2.2. Electrochemical characterization

The electrocatalytic properties of $Ir_xM_{1-x}O_2$ thin films for the OER were assessed first by cyclic voltammetry at 10 $mV.s^{-1}$ in alkaline electrolyte (0.1M NaOH) at T = 22°C. The current density was normalized by the electrochemically active surface area (ECSA), which are reported in Table 2. The ECSA varies between 0.2 and 0.5 cm^2, close to the geometric surface area of the sample (0.28 cm^2). In all cases, the roughness factor, which is given by the ratio of ECSA to geometric surface area, is less than 2, indicating that all the films are relatively smooth. This is consistent with the RMS roughness determined by AFM on IrO_2 and $Ir_{0.85}Ni_{0.15}O_2$. A series of 40 CVs at 10 $mV\ s^{-1}$ were realized first (not shown), followed by CVs at 1 $mV\ s^{-1}$. They are displayed in Figure 5A and 5B for (100)-oriented $Ir_{1-x}M_xO_2$ thin films with different M. Ni substitution of Ir gives the most active compound. Figure 5C compares the potential measured at j = 10 µA cm_{ox}^{-2}, which we refer to as the onset potential. This potential is more than 50 mV lower for $Ir_{0.85}Ni_{0.15}O_2$ than pure IrO_2. At 1.63 V (Figure 5D), which corresponds to an overpotential of 400 mV, films substituted by Ni, W, Mo and Mn exhibit larger current densities than unsubstituted IrO_2. Films substituted by V and Cr generate similar current density as unsubstituted IrO_2. Again, substitution of 15 at.% Ir by Ni yields the best performance, with a current density that is a factor 18 larger than for the IrO_2 parent compound. It should be reiterated that all films are atomically smooth with (100) surface orientation. Any significant difference in OER activity can therefore be attributed to the variation in atomic composition.

2.3. DFT calculations

To understand the OER characteristics determined experimentally and explain why the onset potential of the OER varies with M, a three-layer (100) slab of $Ir_{0.75}M_{0.25}O_2$ with a vacuum layer of about 15 Å was created to model the surface (see Figure S3). The activity for the OER depends on the electronic band structure at the catalyst surface. After optimized structures of $Ir_{1-x}M_xO_2$ (100) slabs were obtained, chemisorbed reaction intermediates (O*, OH* and OOH*) were added to preferred adsorption site (see Figure S3).The reaction pathway was reconstructed from reaction energies involved in the formation of and transformation between these intermediates as well as the formation of the final product, which are calculated by DFT. From these DFT calculations, the potential-determining step can be identified, which is defined as the step with maximum change in the Gibbs free energy of chemisorption between two subsequent adsorbed intermediates, with $\eta_{DFT} = \left(\frac{\Delta G_{max}}{e}\right) - 1.23$ V. At the potential U = 1.23 + η_{DFT}, all steps are exothermic (see Figure S3). Chemisorption of the OER intermediates were only considered on the cationic site, since the implication of the anionic network in the OER is negligible on crystalline rutile IrO_2, in contrast to the hydrated amorphous form of iridium oxide. [52, 53]

In Figure 6A, the values of η_{DFT} are plotted over the adsorption energy difference between *OH and *O on the M site and iridium site for $Ir_{0.75}M_{0.25}O_2$.The variation of η_{DFT} with ΔE (MOOH – MO) - ΔE (IrOOH - IrO) displays a peaked shape (or volcano shape). Substitution of Ir by Ni has the largest impact on η_{DFT}, which changes from -0.96 V to -0.49 V upon Ni substitution. The largest increases of η_{DFT} are seen with Sn and W as Ir substituents, which exhibit the lowest negative and highest positive value of ΔE (MOOH – MO) - ΔE (IrOOH – IrO), respectively. The reasons underlying this effect can be best appreciated by looking at Figure S4, where energy level diagrams are plotted for IrO_2, $Ir_{0.75}Ni_{0.25}O_2$, $Ir_{0.75}Sn_{0.25}O_2$, $Ir_{0.75}W_{0.25}O_2$ and an ideal catalyst. Sn-doped IrO_2 binds the *O intermediate too weakly, while W-doped IrO_2 binds *OH and *O intermediates too strongly. In contrast, Ni-doped IrO_2 is a better catalyst for the OER because it binds the *OH intermediate less strongly than undoped IrO_2, approaching the 1.23 eV binding energy level of an ideal catalyst.

Song *et al* [54] have performed first-principles calculations to predict the OER onset potentials of a series of $Ir_{0.5}M_{0.5}O_2$ rutile-type bulk structure with (110) surface termination. Although both the composition (x = 0.5 instead of 0.25) and the surface termination ((110) instead of (100)) are different, both set of results agree on the relative effect of M on the calculated onset potential for M = Cr, Mn, Ru, Pt and Sn, with the exception of M = Rh. They did not investigate the case of M = Ni.

As noted elsewhere, metals and oxide surfaces exhibit a 3.2 eV difference between the adsorption energies of HO* and HOO*, regardless of the binding site [55]. This constant energy difference is a manifestation of a “scaling law”. The scaling law imposes a minimum theoretical value of η_{DFT}= 0.4 V [11]. Among the eleven different metals considered, substitution of Ir by Ni results in the closest approach to this theoretical limit, with η_{DFT} = -0.49 V at ΔE (MOOH – MO) - ΔE (IrOOH - IrO) = -0.24 eV. It will be an interesting question for future studies to explore if the theoretical limit of η_{DFT} could be approached more closely upon further optimization of the oxide alloy composition and atomic configuration.

For comparison, experimentally measured onset potentials are plotted in Figure 6B over the values of ΔE (MOOH – MO) - ΔE (IrOOH - IrO), which have been calculated with DFT. Both modeling and experimental data for the onset potential display the same trend with respect to ΔE (MOOH – MO) - ΔE (IrOOH - IrO), although the experimental results are more dispersed. The full lines in Figure 6A and 6B were drawn as a guide to the eyes but they have the same shape except for a *Y*-axis scale factor adjustment. Several reasons can be responsible for the observed dispersion in experimental data points: (i) the M content of (100)-oriented $(Ir,M)O_2$ thin films varies among samples and differs from the fixed value of x = 0.25 used in all computations; (ii) as discussed previously, the $(Ir,M)O_2$ thin films prepared by the PLD technique and the slab model used in the DFT calculations have the same [100] growth direction. However, as seen in Figure 3, the intensity of the (200) XRD peak varies with M, being the highest for unsubstituted IrO_2 and the lowest for Mn-substituted (100)-oriented $Ir_{1-x}M_xO_2$ thin films. Part of this variation can be accounted for based on variations in film thicknesses and scattering form factors (different film composition) of the rutile unit cell. Variation of crystallinity between films cannot be completely excluded, although the XRD traces are all flat with no hints to the presence of amorphous phases; and (iii) the DFT calculations performed in the present study do not capture the activation barriers of the different elementary reaction steps. Considering these factors, the agreement between the experimental and modeling results is remarkable, emphasizing the predictive power of DFT modelling and the ability of the PLD technique to prepare well-defined and reproducible films that are structurally and compositionally close to the modelling conditions.

Substitution of Ir by Ni has the biggest impact on the onset potential for the OER. Not surprisingly, this translates into a current density j at 1.63 V *vs* RHE that is a factor of 18 larger for the Ni-doped sample than for undoped IrO_2. As observed by XPS (Figure S6 and Table S1) there is a Ni enrichment at the surface of the film compare to the bulk value. Before OER, the main component of the Ir $4f_{7/2}$ core level peak of (100)-oriented IrO_2 is at *ca* 62.0 eV. Upon alloying with Ni, there is a slight shift of the main component to *ca* 61.7 eV. The Ni $2p_{3/2}$ core level exhibits a major component at *ca* 855.4 eV, with a shoulder at *ca* 854.1 eV. After OER, there is no change in the Ir $4f_{7/2}$ and Ni $2p_{3/2}$ core level peaks of (100)-oriented $Ir_{0.85}Ni_{0.15}O_2$. There is not trace of any metallic Ni^0 and Ir^0, whose peaks are expected at 60.9 and 852.6 eV, respectively. The Ir and Ni content is the same before and after OER, indicating that metal leaching is not occurring on the time scale of these experiments. We would like to emphasize that the $Ir_{1-x}Ni_xO_2$ thin films under investigation here are different from previous reports, where the focus was on the OER characteristics of materials made of metallic IrNi alloys that were then further oxidized, followed by dissolution of nickel in an acidic media [19, 36-42]. This subsequent oxidation reaction must lead to a total reorganization of the electrode surface, which could then bear no resemblance to the well organized and regularly spaced atomic arrangement of the slab model used for DFT calculations. In contrast, the present study provides clear evidence of the formation of a well-defined oxide alloy with the same rutile structure as undoped IrO_2. Moreover, using the PLD technique, we were able to grow epitaxial $Ir_{1-x}Ni_xO_2$ layers with (100) surface orientation that matches the slab model used for the DFT calculations.

The data of Figure 5D show that (100)-oriented $Ir_{1-x}M_xO_2$ thin films with M = Cr, W, Mo, Mn and V have *j* values that are on par and even larger than undoped IrO_2, even if they are characterized by lower onset potential values. This must reflect a variation of the Tafel slopes with M, and thus of the reaction mechanisms of the OER. The case of W is particularly intriguing since W is stable in acid media, opening up the prospect of forming inert (100)-oriented $Ir_{1-x}W_xO_2$ anodes for the OER in acidic environment. In that respect, it would be interesting to investigate M = Nb and Ti, since they are also known to be stable in acids.

IrO_2 with (100) surface termination is the facet with the highest electrocatalytic activity for the OER. However, the facet preference might not the same for $Ir_{1-x}M_xO_2$; further DFT calculations on the effect of M on the activity of different (hkl) surface terminations are underway. As stated earlier, the PLD technique allows for the preparation of IrO_2 thin films with different (hkl) facets and a concomitant experimental verification of the DFT modeling results could readily be achieved if it turns out that the most active facets of $Ir_{1-x}M_xO_2$ thin films change with the nature and level of doping.

3. Conclusions

In conclusion, our aim in undertaking this work was to find a way to prepare electrodes that would be as close as possible to slab models used to perform DFT calculations, which provide a high level of control over the atomic arrangement. To assess the effect of doping on the intrinsic OER characteristic of IrO_2, the Pulsed Laser deposition (PLD) technique was used to synthetize a series of Ir-based oxide alloys, $Ir_{1-x}M_xO_2$, with M = Ni, Cr, Mo, W, Sn, Pt, Rh, Ru, V and Mn. Epitaxial growth along the [100] growth axis was achieved in all cases, which is the most active facet of undoped IrO_2. All films are atomically smooth and the assessment of the doping effect was achieved through comparison of the intrinsic OER characteristics of the films. Substitution of Ir by Ni gives the best results, with a 50 mV decrease of the onset potential and 18-fold increase of the current density at 400 mV overpotential. This is mostly accomplished with the increase of the binding energy of the *OH intermediate.

Doping of IrO_2 with Mo also led to a 2-fold increase of the current density at the same overpotential and more investigation of this system is underway. Finally, it would be interesting to investigate if the scaling law that is responsible for the minimum attainable theoretical onset potential can be broken by investigating quaternary oxide alloy (Ir,M,N,O). It is foreseen that (100)-oriented (Ir,M,N,O), where M and N are two distinct elements, could be readily prepared by PLD, providing an experimental platform to further scrutinize and exploit the predictive capabilities of DFT calculations.

Finally, showing Ni at the top and other trends being consistent among Figure 6A and 6B, there is nevertheless a huge discrepancy between variations in the thermodynamic overpotential from DFT (2 V variation range in Figure 6A) and the experimental onset potential (0.1 V variation range in Figure 6B). The thermodynamic overpotential from DFT is based on the concept of a potential-determining step, which is controversial for a multistep and multi-pathway process such as the OER. There is a correlation or correspondence between data plotted in Figure 6A and 6B and we should be able to derive or explain this theoretically, but this would require solutions and full parameterization of microkinetic models. This will be achieved in a forthcoming study.

Experimental condition

Thin film synthesis

Mixed Iridium – Metal oxide thin films were deposited by reactive Pulsed Laser Deposition (PLD) in a custom-made stainless-steel vacuum chamber turbo-pumped to a base pressure of 10^{-5} Torr and then filled with 100 mTorr of O_2. The laser beam (KrF, 248 nm, 17 ns pulse width, 20 Hz repetition rate, 60,000 pulses) was focused on the target. The latter was composed of an iridium metal target (99.9%, Kurt J. Lesker Company) that was partially covered (25% of the target area) by a metal foil (Mo 99.95%, Pt 99.99% and Ni 99.994% from Alfa Aeasar, and V 99.7% from Aldrich). Alternatively, the target was made of a metal (W 99.95%, Sn 99.99%, Rh 99.8%, Cr 99.95%, Ru 99.95% and Mn 99.95% from Kurt J. Lesker) that was partially covered (75% of the target area) by an iridium metal foil (99.8%, Alfa Aesar). The target was kept in a continuous rotational and translational motion for uniform ablation, and was kept at an equal distance (5.5 cm) from the substrate. The substrates were made of commercially available (100)-oriented $SrTiO_3$ crystals (10 mm x 10 mm x 0.5 mm, epi polished, MTI Corporation). Before deposition, the substrates were cleaned successively by sonication in isopropanol (15 min) and then acetone (15 min), before being dried under an argon stream. During deposition, the substrate temperature was kept constant at 600°C.

Thin film characterization

Thin film structural characterization was performed by x-ray diffraction with a four circle PANalytical X'pert Pro diffractometer using the Cu $K\alpha_{1+2}$ radiation in $\theta/2\theta$ Bragg-Brentano mode (step size of 0.016° and 1 s $step^{-1}$). The thickness of each film was measured by x-ray reflectivity measurements performed by varying the incident angle from 0.1° to 4° every 0.005° (1 s $step^{-1}$). The chemical composition was measured by Energy-Dispersive X-ray spectroscopy (EDX) with a Bruker Quantax detector on a Scanning Electron Microscopy Tescan Vega3 LMH.

Surface morphologies were obtained via atomic force microscopy (AFM, Smart SPM1000-AIST-NT Inc.), with images acquired in intermittent mode. An AIST-NT Smart system in an acoustic enclosure on an active anti-vibration support was operated with an aluminum coated n-type silicon cantilever (HQ:NSC15/Al BS) from MikroMasch, with nominal values (tip radius of 8 nm, a force constant of 40 N/m and a resonance frequency of 325 kHz).

X-ray photoelectron spectroscopy (XPS) measurements were carried out with a VG Escalab 220i-XL spectrometer using a monochromatic Al Kα radiation (1486.6 eV). The analyzed area of the samples was 250 x 1000 μm^2. The pressure in the analysis chamber was around 1.10^{-9} mbar. Scan survey spectra were recorded using constant pass energy of 100 eV whereas high-resolution spectra of Ir 4f and Ni 2p core levels were collected with a constant pass energy of 20 eV at $\theta = 0°$ take-off angle (angle between the surface normal and the detection direction). The binding energy scale was calibrated from the hydrocarbon contamination using the C 1s peak at 284.6 eV. All spectra were analysed using CasaXPS software (Casa Softw. Ltd, 2005). Core peaks were analysed using a nonlinear Shirley-type background.

Electrochemical characterization

For the electrochemical measurements, ultrapure water (Millipore Gradient, MilliQ, resistivity ≥ 18.2 MΩ cm) was used to clean glassware and to prepare the electrolyte. All glassware was cleaned by immersion overnight into an aqueous H_2SO_4/$KMnO_4$ solution. Then, after rinsing, the glassware was boiled in a nitric acid solution followed by boiling several times in MilliQ water. All electrochemical measurements were carried out in a homemade 4 mL one cell-compartment [56]. The reference electrode (Mercury – Mercury Oxide Hg/HgO) was located in an external compartment that was separated and connected to the main cell by a Luggin capillary. A gold wire situated outside the cell and in contact with the thin film was used as a current collector and a platinum mesh, which was previously flame-annealed and quenched in water, was used as a counter-electrode. Sodium hydroxide (NaOH 99.99%, Alfa Aesar) was used as electrolyte with a 0.1M concentration. The electrolyte was purged for 10 minutes with high-purity argon before the measurements. The (100) $SrTiO_3$ substrate is an insulator and the samples could not be accommodated in a rotating disk electrode setup. To avoid bubble formation at the surface of the sample and to assure reproducible mass transfer, an argon gas flow close to the surface of the sample was used during the electrochemical measurements. After measurements, the potential of the reference electrode was calibrated against a hydrogen electrode, using the same electrolyte from the same batch, and then converted into the RHE scale. All measurements were carried out with a BioLogic VSP potentiostat, equipped with a low-current option and controlled by EC-Lab software. The electrochemically active surface area (EASA) was measured by cyclic voltammetry measurements at different scan rates in a potential window of ± 0.05 V around the open-circuit potential (OCP), in line with McCrory *et al.* [8]. The exposed geometric surface area was 0.28 cm^2.

DFT Calculation

Vienna Ab Initio Simulation Package (VASP) was used to perform the DFT calculations [57-60]. All calculations were based on the Projector Augmented Wave (PAW) method [61]. According to the PAW method, core electrons were kept frozen and replaced by pseudopotentials (Ir, M, O, H) and valence electrons (Ir: 6s2 5d7; O: 2s2 2p4; H: 1s1) are expanded in a plane wave basis set with a kinetic energy cut-off of 400 eV. The ionic relaxation loop would terminate once the forces on all atoms are less than 0.01 eV/Å. Exchange-correlation effects were incorporated within the generalized gradient approximation (GGA), using the functional by Perdew, Burke, and Ernzerhof (PBE) [62]. The Brillouin zone is sampled using Monkhorst−Pack [63] scheme using 6 x 6 x 8 k-points for the bulk and 4 x 4 x 1 k-points for the slab calculations.

Acknowledgement

This research was conducted as part of the Engineered Nickel Catalysts for Electrochemical Clean Energy project administered from Queen’s University and supported by Grant No. RGPNM 477963-2015 under the Natural Sciences and Engineering Research Council of Canada (NSERC) Discovery Frontiers Program.

Supporting Information Available:

S1, Crystalline structure IrO_2, $Ir_{0.75}M_{0.25}O_2$ and (100)-oriented $Ir_{0.75}M_{0.25}O_2$. S2, AFM image IrO_2, $Ir_{0.85}Ni_{0.15}O_2$. S3, OER energy diagram of $Ir_{0.75}M_{0.25}O_2$. S4, OER energy diagram for M = Sn, Ni, W. S5, Scaling relationship between the binding energy values. S6, XPS spectra IrO_2, $Ir_{0.85}Ni_{0.15}O_2$. Table S1, XPS quantification $Ir_{0.85}Ni_{0.15}O_2$.

Notes

The authors declare no competing financial interest.

Reference

1. Benson, E.E.; C.P. Kubiak; A.J. Satrhum; J.M. Smieja, *Electrocatalytic and Homogeneous Approches to Conversion of CO2 to Liquid Fuels,* Chem. Soc. Rev., **2009**, 38, 89 - 99
2. Cook, T.R.; D.K. Dogutan; S.Y. Reece; Y. Surendranath; T.S. Teets; D.G. Nocera, *Solar Energy Supply and Storage for the Legacy and Nonlegacy Worlds,* Chem. Rev., **2010**, 110(11), 6474-6502
3. Turner, J.A., *Sustainable Hydrogen Production,* Science, **2004**, 305(5686), 972-974
4. Carmo, M.; D.L. Fritz; J. Mergel; D. Stolten, *A Comprehensive Review on PEM Water Electrolysis,* Int. J. Hydrogen Energy, **2013**, 38(12), 4901-4934
5. Reier, T.; H.N. Nong; D. Teschner; R. Schlögl; P. Strasser, *Electrocatalytic Oxygen Evolution Reaction in Acidic Environments – Reaction Mechanisms and Catalysts,* Adv. Eng. Mater., **2017**, 7(1), 1601275
6. Reier, T.; M. Oezaslan; P. Strasser, *Electrocatalytic Oxygen Evolution Reaction (OER) on Ru, Ir, and Pt Catalysts: A Comparative Study of Nanoparticles and Bulk Materials,* ACS Catal., **2012**, 2(8), 1765-1772
7. Cherevko, S.; S. Geiger; O. Kasian; N. Kulyk; J.-P. Grote; A. Savan; B.R. Shrestha; S. Merzlikin; B. Breitbach; A. Ludwig; K.J.J. Mayrhofer, *Oxygen and Hydrogen Evolution Reactions on Ru, RuO2, Ir, and IrO2 Thin Film Electrodes in Acidic and Alkaline Electrolytes: A Comparative Study on Activity and Stability,* Catal. Today, **2016**, 262, 170-180
8. McCrory, C.C.L.; S. Jung; J.C. Peters; T.F. Jaramillo, *Benchmarking Heterogeneous Electrocatalysts for the Oxygen Evolution Reaction,* J. Am. Chem. Soc., **2013**, 135(45), 16977-16987
9. Payne, D., *Iridium's impact,* Nat. Chem., **2016**, 8, 392

10. Stoerzinger, K.A.; L. Qiao; M.D. Biegalski; Y. Shao-Horn, *Orientation-Dependent Oxygen Evolution Activities of Rutile IrO2 and RuO2,* J. Phys. Chem. Lett., **2014**, 5(10), 1636-1641
11. Man, I.C.; H.-Y. Su; F. Calle-Vallejo; H.A. Hansen; J.I. Martínez; N.G. Inoglu; J. Kitchin; T.F. Jaramillo; J.K. Nørskov; J. Rossmeisl, *Universality in Oxygen Evolution Electrocatalysis on Oxide Surfaces,* ChemCatChem, **2011**, 3(7), 1159-1165
12. Rodriguez, J., *Physical and chemical properties of bimetallic surfaces,* Surf. Sci. Rep., **1996**, 24(7), 223-287
13. Kitchin, J.R.; J.K. Nørskov; M.A. Barteau; J.G. Chen, *Role of Strain and Ligand Effects in the Modification of the Electronic and Chemical Properties of Bimetallic Surfaces,* Phys. Rev. Lett., **2004**, 93(15), 156801
14. Mueller, J.E.; P. Krtil; L.A. Kibler; T. Jacob, *Bimetallic alloys in action: dynamic atomistic motifs for electrochemistry and catalysis,* Phys. Chem. Chem. Phys., **2014**, 16(29), 15029-15042
15. Escudero-Escribano, M.; K.D. Jensen; A.W. Jensen, *Recent advances in bimetallic electrocatalysts for oxygen reduction: design principles, structure-function relations and active phase elucidation,* Current Opinion in Electrochemistry, **2018**, 8, 135-146
16. Stamenkovic, V.R.; B.S. Mun; M. Arenz; K.J.J. Mayrhofer; C.A. Lucas; G. Wang; P.N. Ross; N.M. Markovic, *Trends in electrocatalysis on extended and nanoscale Pt-bimetallic alloy surfaces,* Nature Materials, **2007**, 6(3), 241-247
17. Greeley, J.; I.E.L. Stephens; A.S. Bondarenko; T.P. Johansson; H.A. Hansen; T.F. Jaramillo; J. Rossmeisl; I. Chorkendorff; J.K. Nørskov, *Alloys of platinum and early transition metals as oxygen reduction electrocatalysts,* Nat. Chem., **2009**, 1(7), 552-556
18. Stamenkovic, V.R.; B. Fowler; B.S. Mun; G. Wang; P.N. Ross; C.A. Lucas; N.M. Marković, *Improved Oxygen Reduction Activity on Pt<sub>3</sub>Ni(111) via Increased Surface Site Availability,* Science, **2007**, 315(5811), 493
19. Reier, T.; Z. Pawolek; S. Cherevko; M. Bruns; T. Jones; D. Teschner; S. Selve; A. Bergmann; H.N. Nong; R. Schlögl; K.J.J. Mayrhofer; P. Strasser, *Molecular Insight in Structure and Activity of Highly Efficient, Low-Ir Ir–Ni Oxide Catalysts for Electrochemical Water Splitting (OER),* J. Am. Chem. Soc., **2015**, 137(40), 13031-13040
20. Vos, J.G.; T.A. Wezendonk; A.W. Jeremiasse; M.T.M. Koper, *MnOx/IrOx as Selective Oxygen Evolution Electrocatalyst in Acidic Chloride Solution,* J. Am. Chem. Soc., **2018**, 140(32), 10270-10281
21. Zhou, Z.; W.Q. Zaman; W. Sun; L.-m. Cao; M. Tariq; J. Yang, *Cultivating Crystal Lattice Distortion in IrO2 via Coupling with MnO2 to Boost the Oxygen Evolution Reaction with High Intrinsic Activity,* Chem. Commun., **2018**, 54(39), 4959-4962
22. Tariq, M.; W.Q. Zaman; W. Sun; Z. Zhou; Y. Wu; L.-m. Cao; J. Yang, *Unraveling the Beneficial Electrochemistry of IrO2/MoO3 Hybrid as a Highly Stable and Efficient Oxygen Evolution Reaction Catalyst,* ACS Sustain. Chem. Eng., **2018**, 6(4), 4854-4862

23. Bhanja, P.; B. Mohanty; A.K. Patra; S. Ghosh; B.K. Jena; A. Bhaumik, *IrO2 and Pt Doped Mesoporous SnO2 Nanospheres as Efficient Electrocatalysts for the Facile OER and HER,* ChemCatChem, **2019**, 11(1), 583-592
24. De Pauli, C.P.; S. Trasatti, *Electrochemical Surface Characterization of IrO2 + SnO2 Mixed Oxide Electrocatalysts,* J. Electroanal. Chem., **1995**, 396(1), 161-168
25. Xu, J.; G. Liu; J. Li; X. Wang, *The Electrocatalytic Properties of an IrO2/SnO2 Catalyst Using SnO2 as a Support and an Assisting Reagent for the Oxygen Evolution Reaction,* Electrochim. Acta, **2012**, 59, 105-112
26. Tariq, M.; W.Q. Zaman; Y. Wu; A. Nabi; Z. Abbas; W. Iqbal; W. Sun; Z. Hao; Z.H. Zhou; L. Cao; J. Yang, *Facile Synthesis of IrO2 Nanoparticles Decorated @ WO3 as Mixed Oxide Composite for Outperformed Oxygen Evolution Reaction,* Int. J. Hydrogen Energy, **2019**, 44(59), 31082-31093
27. Kumari, S.; B.P. Ajayi; B. Kumar; J.B. Jasinski; M.K. Sunkara; J.M. Spurgeon, *A Low-Noble-Metal W1−xIrxO3−δ Water Oxidation Electrocatalyst for Acidic Media via Rapid Plasma Synthesis,* Ener. Env. Sci., **2017**, 10(11), 2432-2440
28. Escudero-Escribano, M.; A.F. Pedersen; E.A. Paoli; R. Frydendal; D. Friebel; P. Malacrida; J. Rossmeisl; I.E.L. Stephens; I. Chorkendorff, *Importance of Surface IrOx in Stabilizing RuO2 for Oxygen Evolution,* J. Phys. Chem. B, **2018**, 122(2), 947-955
29. Gou, W.; M. Zhang; Y. Zou; X. Zhou; Y. Qu, *Iridium-Chromium Oxide Nanowires as Highly Performed OER Catalysts in Acidic Media,* ChemCatChem, **2019**, 11(24), 6008-6014
30. Papazisi, K.M.; A. Siokou; S. Balomenou; D. Tsiplakides, *Preparation and Characterization of IrxPt1−xO2 Anode Electrocatalysts for the Oxygen Evolution Reaction,* Int. J. Hydrogen Energy, **2012**, 37(21), 16642-16648
31. Audichon, T.; E. Mayousse; S. Morisset; C. Morais; C. Comminges; T.W. Napporn; K.B. Kokoh, *Electroactivity of RuO2–IrO2 Mixed Nanocatalysts Toward the Oxygen Evolution Reaction in a Water Electrolyzer Supplied by a Solar Profile,* Int. J. Hydrogen Energy, **2014**, 39(30), 16785-16796
32. Lee, S.W.; C. Baik; T.-Y. Kim; C. Pak, *Three-Dimensional Mesoporous Ir–Ru Binary Oxides with Improved Activity and Stability for Water Electrolysis,* Catal. Today, **2019**, *In Press (https://doi.org/10.1016/j.cattod.2019.10.004)*
33. Marshall, A.; B. Børresen; G. Hagen; M. Tsypkin; R. Tunold, *Electrochemical Characterisation of IrxSn1−xO2 Powders as Oxygen Evolution Electrocatalysts,* Electrochim. Acta, **2006**, 51(15), 3161-3167
34. Li, G.; H. Yu; X. Wang; S. Sun; Y. Li; Z. Shao; B. Yi, *Highly Effective IrxSn1−xO2 Electrocatalysts for Oxygen Evolution Reaction in the Solid Polymer Electrolyte Water Electrolyser,* Phys. Chem. Chem. Phys., **2013**, 15(8), 2858-2866
35. Zaman, W.Q.; Z. Wang; W. Sun; Z. Zhou; M. Tariq; L. Cao; X.-Q. Gong; J. Yang, *Ni–Co Codoping Breaks the Limitation of Single-Metal-Doped IrO2 with Higher Oxygen Evolution Reaction Performance and Less Iridium,* ACS Energy Lett., **2017**, 2(12), 2786-2793
36. Strickler, A.L.; R.A. Flores; L.A. King; J.K. Nørskov; M. Bajdich; T.F. Jaramillo, *Systematic Investigation of Iridium-Based Bimetallic Thin Film Catalysts for the*

Oxygen Evolution Reaction in Acidic Media, ACS Appl. Mat. Int., **2019**, 11(37), 34059-34066

37. Nong, H.N.; T. Reier; H.-S. Oh; M. Gliech; P. Paciok; T.H.T. Vu; D. Teschner; M. Heggen; V. Petkov; R. Schlögl; T. Jones; P. Strasser, *A Unique Oxygen Ligand Environment Facilitates Water Oxidation in Hole-Doped IrNiOx Core–Shell Electrocatalysts,* Nat. Catal., **2018**, 1(11), 841-851
38. Özer, E.; I. Sinev; A.M. Mingers; J. Araujo; T. Kropp; M. Mavrikakis; K.J.J. Mayrhofer; B.R. Cuenya; P. Strasser, *Ir-Ni Bimetallic OER Catalysts Prepared by Controlled Ni Electrodepostion on Irpoly and Ir(111),* Surfaces, **2018**, 1(1), 165 - 186
39. Touni, A.; A. Papaderakis; D. Karfaridis; G. Vourlias; S. Sotiropoulos, *Oxygen Evolution Reaction at IrO2/Ir(Ni) Film Electrodes Prepared by Galvanic Replacement and Anodization: Effect of Precursor Ni Film Thickness,* Molecules, **2019**, 24(11), 2095
40. Papaderakis, A.; N. Pliatsikas; C. Prochaska; G. Vourlias; P. Patsalas; D. Tsiplakides; S. Balomenou; S. Sotiropoulos, *Oxygen Evolution at IrO2 Shell–Ir−Ni Core Electrodes Prepared by Galvanic Replacement,* J. Phys. Chem. C, **2016**, 120(36), 19995-20005
41. Godínez-Salomón, F.; L. Albiter; S.M. Alia; B.S. Pivovar; L.E. Camacho-Forero; P.B. Balbuena; R. Mendoza-Cruz; M.J. Arellano-Jimenez; C.P. Rhodes, *Self-Supported Hydrous Iridium–Nickel Oxide Two-Dimensional Nanoframes for High Activity Oxygen Evolution Electrocatalysts,* ACS Catal., **2018**, 8(11), 10498-10520
42. Nong, H.N.; H.-S. Oh; T. Reier; E. Willinger; M.-G. Willinger; V. Petkov; D. Teschner; P. Strasser, *Oxide-Supported IrNiOx Xore-Shell Particles as Efficient, Cost-Effective, and Stable Catalysts for Electrochemical Water Splitting,* Angew. Chem. Int. Ed., **2015**, 54(10), 2975 - 2979
43. Sung, M.; J. Kim, *Oxygen Evolution Reaction on Pt Sphere and Ir-Modified Pt Sphere Electrodes with Porous Structures,* Int. J. Hydrogen Energy, **2018**, 43(4), 2130-2138
44. Li, C.; Y. Xu; S. Liu; S. Yin; H. Yu; Z. Wang; X. Li; L. Wang; H. Wang, *Facile Construction of IrRh Nanosheet Assemblies As Efficient and Robust Bifunctional Electrocatalysts for Overall Water Splitting,* ACS Sustain. Chem. Eng., **2019**, 7(18), 15747-15754
45. Guo, H.; Z. Fang; H. Li; D. Fernandez; G. Henkelman; S.M. Humphrey; G. Yu, *Rational Design of Rhodium–Iridium Alloy Nanoparticles as Highly Active Catalysts for Acidic Oxygen Evolution,* ACS Nano, **2019**, 13(11), 13225-13234
46. Lv, F.; J. Feng; K. Wang; Z. Dou; W. Zhang; J. Zhou; C. Yang; M. Luo; Y. Yang; Y. Li; P. Gao; S. Guo, *Iridium–Tungsten Alloy Nanodendrites as pH-Universal Water-Splitting Electrocatalysts,* ACS Cent. Sci., **2018**, 4(9), 1244-1252
47. Fu, L.; X. Hu; Y. Li; G. Cheng; W. Luo, *IrW Nanobranches as an Advanced Electrocatalyst for pH-Universal Overall Water Splitting,* Nanoscale, **2019**, 11(18), 8898-8905
48. Sacré, N.; M. Duca; S. Garbarino; R. Imbeault; A. Wang; A. Hadj Youssef; J. Galipaud; G. Hufnagel; A. Ruediger; L. Roué; D. Guay, *Tuning Pt–Ir Interactions for NH3 Electrocatalysis,* ACS Catal., **2018**, 8(3), 2508-2518

49. Duca, M.; N. Sacré; A. Wang; S. Garbarino; D. Guay, *Enhanced Electrocatalytic Nitrate Reduction by Preferentially-Oriented (100) PtRh and PtIr Alloys: the Hidden Treasures of the 'Miscibility Gap'*, Appl. Catal. B-Environ., **2018**, 221, 86-96
50. Eason, R., *Pulsed Laser Deposition of Thin Films - Applications-Led Growth of Functional Materials*. 2006: Wiley-Interscience.
51. Buvat, G.; M.J. Eslamibidgoli; A.H. Youssef; S. Garbarino; A. Ruediger; M. Eikerling; D. Guay, *Effect of IrO6 Octahedron Distortion on the OER Activity at (100) IrO2 Thin Film*, ACS Catal., **2020**, 10(1), 806-817
52. Geiger, S.; O. Kasian; M. Ledendecker; E. Pizzutilo; A.M. Mingers; W.T. Fu; O. Diaz-Morales; Z. Li; T. Oellers; L. Fruchter; A. Ludwig; K.J.J. Mayrhofer; M.T.M. Koper; S. Cherevko, *The stability number as a metric for electrocatalyst stability benchmarking,* Nat. Catal., **2018**, 1(7), 508-515
53. Kasian, O.; S. Geiger; T. Li; J.-P. Grote; K. Schweinar; S. Zhang; C. Scheu; D. Raabe; S. Cherevko; B. Gault; K.J.J. Mayrhofer, *Degradation of iridium oxides via oxygen evolution from the lattice: correlating atomic scale structure with reaction mechanisms,* Ener. Env. Sci., **2019**, 12(12), 3548-3555
54. Song, Y.; J. Yang; X.-Q. Gong, *Prediction of Ir0.5M0.5O2 (M = Cr, Ru or Pb) Mixed Oxides as Active Catalysts for Oxygen Evolution Reaction from First-Principles Calculations,* Top. Catal., **2015**, 58(10), 675-681
55. M., K.M.T., *Thermodynamic Theory of Multi-Electron Transfer Reactions: Implications for Electrocatalysis,* J. Electroanal. Chem., **2011**, 660(2), 254-260
56. Martin, M.H.; J. Galipaud; A. Tranchot; L. Roué; D. Guay, *Measurements of Hydrogen Solubility in CuxPd100−x Thin Films,* Electrochim. Acta, **2013**, 90, 615-622
57. Kresse, G.; J. Furthmüller, *Efficiency of ab-initio Total Energy Calculations for Metals and Semiconductors Using a Plane-Wave Basis Set,* Comput. Mater. Sci., **1996**, 6(1), 15-50
58. Kresse, G.; J. Furthmüller, *Efficient Iterative Schemes for ab initio Total-Energy Calculations Using a Plane-Wave Basis Set,* Phy. Rev. B, **1996**, 54(16), 11169-11186
59. Kresse, G.; J. Hafner, *Ab initio Molecular Dynamics for Liquid Metals,* Phy. Rev. B, **1993**, 47(1), 558-561
60. Kresse, G.; J. Hafner, *Ab initio Molecular-Dynamics Simulation of the Liquid-Metal--Amorphous-Semiconductor Transition in Germanium,* Phy. Rev. B, **1994**, 49(20), 14251-14269
61. Blöchl, P.E., *Projector Augmented-Wave Method,* Phy. Rev. B, **1994**, 50(24), 17953-17979
62. Perdew, J.P.; K. Burke; M. Ernzerhof, *Generalized Gradient Approximation Made Simple,* Phys. Rev. Lett., **1996**, 77(18), 3865-3868
63. Monkhorst, H.J.; J.D. Pack, *Special Points for Brillouin-Zone Integrations,* Phy. Rev. B, **1976**, 13(12), 5188-5192
64. Shannon, R., *Revised Effective Ionic Radii and Systematic Studies of Interatomic Distances in Halides and Chalcogenides,* Acta Crystallogr. Sect. A, **1976**, 32(5), 751-767.

Table 1: Summary of the physico-chemical characterization of $Ir_{1-x}M_xO_2$ thin films

Compound $(Ir,M)O_2$	M content, *x*, from EDX (at. %)	Film thickness from XRR (nm)	Out-of-plane *a* lattice parameter from XRD (Å)	Calculated unit cell lattice parameter *a* from DFT (Å)
IrO_2	-	54.9 ± 2.4	4.4890 ± 0.0001	4.494
$(Ir,Mo)O_2$	21 ± 2	23.6 ± 3.5	4.5559 ± 0.0006	4.529
$(Ir,W)O_2$	13 ± 4	27.2 ± 2.9	4.6186 ± 0.0003	4.528
$(Ir,Sn)O_2$	10 ± 1	67.8 ± 1.6	4.5351 ± 0.0002	4.523
$(Ir,Rh)O_2$	18 ± 1	44.4 ± 3.4	4.4818 ± 0.0001	4.498
$(Ir,Pt)O_2$	29 ± 2	30.0 ± 2.9	4.5283 ± 0.0005	4.514
$(Ir,Cr)O_2$	14 ± 3	25.7 ± 2.6	4.5109 ± 0.0001	4.485
$(Ir,Ru)O_2$	8.7 ± 0.9	28.5 ± 2.9	4.4715 ± 0.0001	4.498
$(Ir,Ni)O_2$	15 ± 4	46.8 ± 4.2	4.4734 ± 0.0004	4.478
$(Ir,Mn)O_2$	31 ± 2	33.0 ± 1.0	4.4566 ± 0.0003	4.448
$(Ir,V)O_2$	46 ± 1	49.5 ± 1.2	4.5031 ± 0.0002	4.506

Table 2: Summary of the OER characteristics of the (Ir,M)O_2 compounds

Compound	x in $Ir_{1-x}M_xO$	Electrochemical Surface Area (cm²)	Overpotential measured at 10 $\mu A.cm^{-2}_{ox}$ (V)	j measured at 1.63 V vs. RHE ($\mu A.cm^{-2}_{ox}$)	η_{DFT} for $Ir_{0.75}M_{0.25}O_2$ (V)
IrO_2	-	0.338 ± 0.005	0.302	119	-0.96
(Ir,Mo)O_2	0.21 ± 0.02	0.408 ± 0.005	0.311	201	-1.05
(Ir,W)O_2	0.13 ± 0.04	0.296 ± 0.005	0.322	133	-1.25
(Ir,Sn)O_2	0.10 ± 0.01	0.313 ± 0.006	0.369	29	-1.82
(Ir,Rh)O_2	0.18 ± 0.01	0.261 ± 0.004	0.347	67	-0.94
(Ir,Pt)O_2	0.29 ± 0.02	0.313 ± 0.006	0.345	57	-1.22
(Ir,Cr)O_2	0.14 ± 0.03	0.239 ± 0.007	0.329	107	-0.88
(Ir,Ru)O_2	0.087 ± 0.009	0.470 ± 0.01	0.341	63	-0.88
(Ir,Ni)O_2	0.15 ± 0.04	0.197 ± 0.006	0.249	2124	-0.49
(Ir,Mn)O_2	0.31 ± 0.02	0.440 ± 0.006	0.329	124	-0.86
(Ir,V)O_2	0.46 ± 0.01	0.577 ± 0.007	0.334	101	-1.06

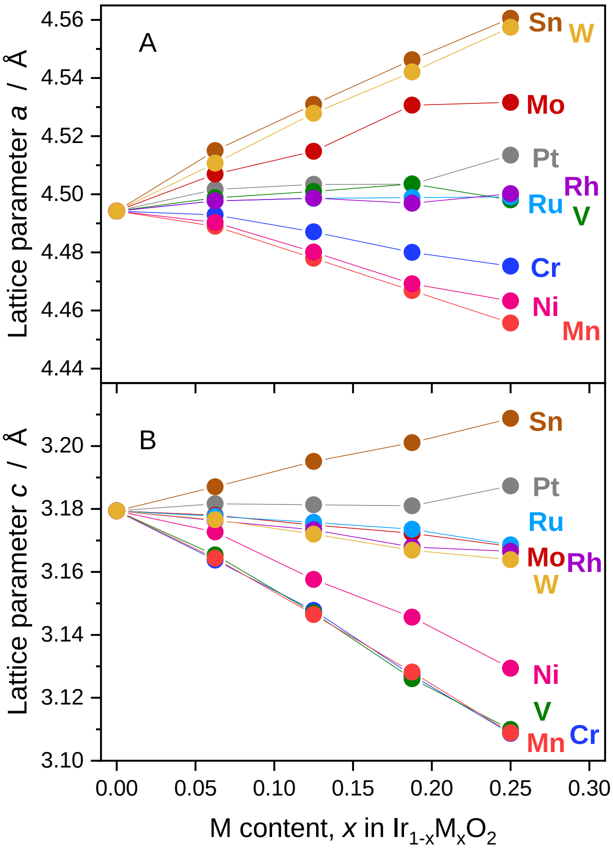

Figure 1 Lattice parameters *a* (A) and *c* (B) for the rutile structure of $Ir_{1-x}M_xO_2$ with different M, plotted against the atomic fraction *x*.

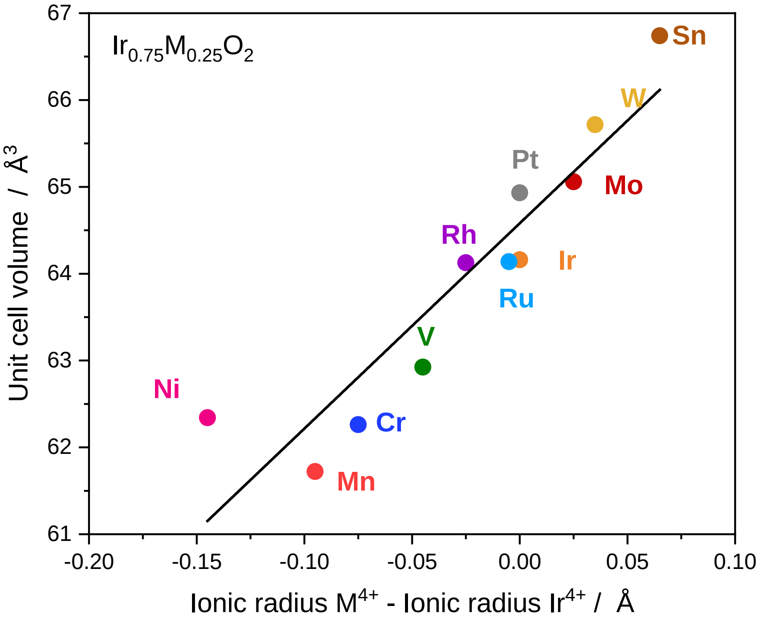

Figure 2 Unit cell volume obtained for different M in $Ir_{0.75}M_{0.25}O_2$, plotted against the difference in ionic radii between M and Ir as reported in the literature [64].

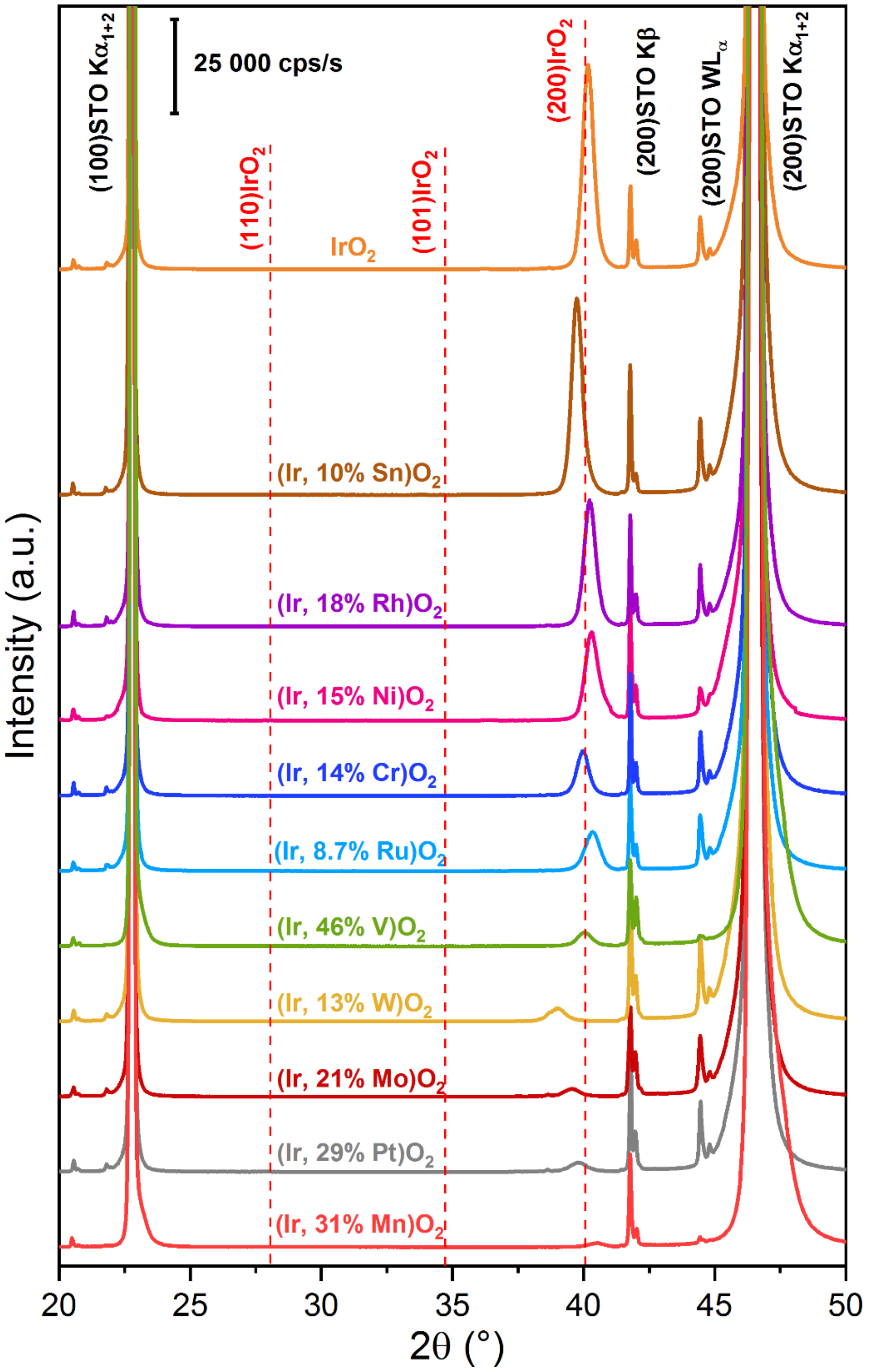

Figure 3 XRD patterns (θ-2θ) of $Ir_{1-x}M_xO_2$ deposited on (100) $SrTiO_3$ single crystal substrate. The M content is indicated. The dotted lines represent the peak positions of bulk IrO_2 according to JCPDS file n° 00-015-0870.

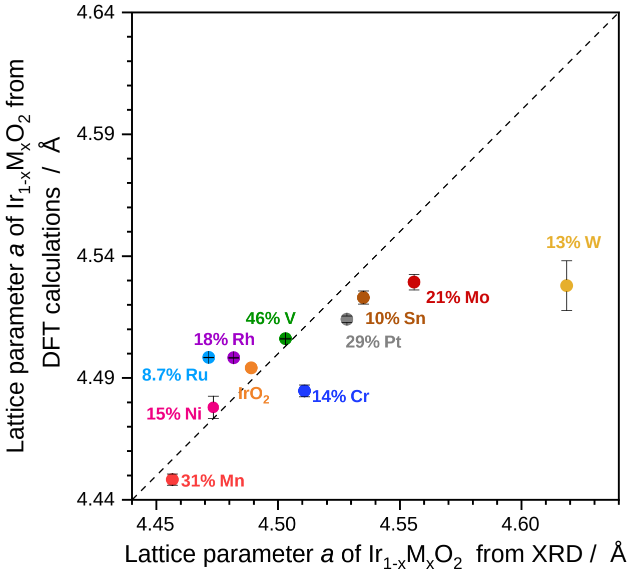

Figure 4 Lattice parameter *a* of $Ir_{1-x}M_xO_2$ from DFT calculations over experimentally measured value of *a*, for the different substituent species M considered in this work. The DFT value of *a* lattice parameter was obtained from a linear interpolation of the data shown in Fig. S1, using the experimentally determined *x* value (M content) of Table 1.

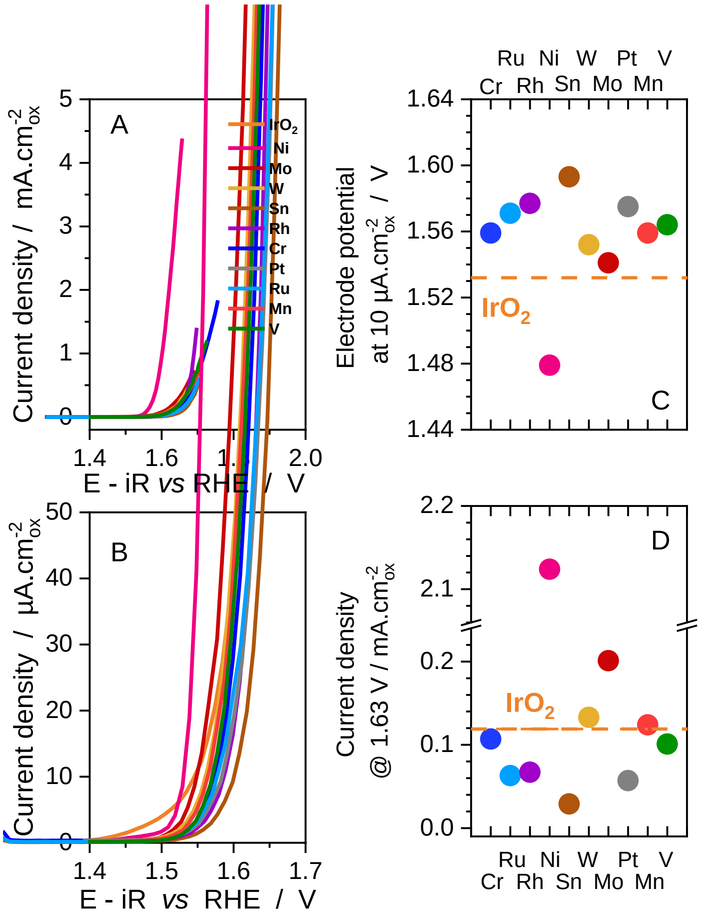

Figure 5 A and B show steady state CV curves in 0.1M NaOH at 1 mV.s^{-1} of (100)-oriented $Ir_{1-x}M_xO_2$ thin films. C shows the electrode potential for the OER at *j* = 10 µA cm$_{ox}^{-2}$ (referred to in the text as "onset potential"). D displays the current density, *j*, measured at a fixed electrode potential of 1.63 V vs. RHE.

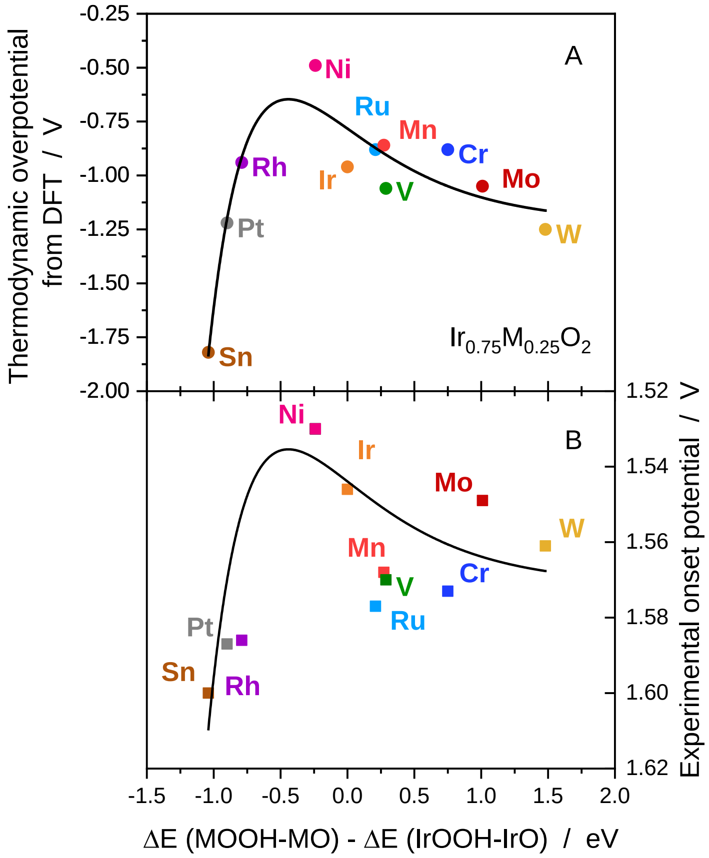

Figure 6 A shows the variation of the thermodynamic overpotential for the OER at $Ir_{0.75}M_{0.25}O_2$, calculated from DFT, plotted over the difference between the adsorption energy of *OH and *O on the iridium site and metal site. B shows the experimental onset potential for the OER at the same materials and plotted vs. the same adsorption energy difference.

Graphic for manuscript